Vortex Wake of Laminar Flow around Two Side-by-Side Elliptic Cylinders

Van Luc Nguyen[1,*], Tan Dung Le[1], and Huynh Duc Le[1]
[1]Faculty of Aeronautical Engineering, Vietnam Aviation Academy, Viet Nam
[*]Corresponding Author / E-mail: lucnv@vaa.edu.vn

Manuscript received: April 16, 2023 / Revised: May 15, 2023 / Accepted: June 20, 2023

ABSTRACT

This study clarifies the characteristics of the vortex wake of flow around two elliptic cylinders in the side-by-side arrangement at a Reynolds number of 100. The cylinders have their axis ratio of 0.5, and their spacing varies from 1.2D to 2.5D, where D is the projection of the cylinder onto the vertical axis. Four flow configurations, such as two normal, convergent, divergent, and same-angle-of-attack elliptic cylinders, are examined. The simulation results show that nine flow patterns can take place, such as steady vortex pair, a single bluff body flow, two anti-phase synchronized Karman vortex streets, two in-phase synchronized vortex streets, two anti-phase synchronized Karman vortex streets followed by steady shear layers, steady shear layers followed by vortices and then a recreation of steady shear layers, steady shear layers followed by a Karman vortex street, flip-flopping wake, and chaotic flow. These patterns significantly depend on the spacing and their configuration.

KEYWORDS: Vortex wake, Flow pattern, Flow around elliptic cylinders, Side-by-side cylinders

NOMENCLATURE

$\boldsymbol{x}$, $\boldsymbol{x}_q$, $\boldsymbol{x}_p$ = Spatial coordinate, locations of the grid and the Lagrangian points
t = *time*
p = Pressure
$\boldsymbol{u}$ = Flow velocity field
$\boldsymbol{u}_S$ = Solid velocity
Re = Reynolds number
Fr = Froude number
D = Projection on the cylinder on the vertical axis
L = Distance between centers of two cylinders
d = Signed distance from the grid node to solid surface
U_∞ = Upstream velocity
Cd and Cl = Drag and lift coefficients
rms_Cl = Root mean square of the lift coefficient
$\boldsymbol{\omega}$ = Vorticity field
$\boldsymbol{\psi}$ = Vector scalar potential of the velocity field
ϕ = Scalar potential of the velocity field
λ = Penalization parameter
χ_S = Solid function
ε = Half of the interface thickness
Superscript '*' = Nondimensional quantity
Subscript 1 and 2 = Lower and upper cylinders

1. Introduction

Flow around solid bluff bodies is observed widely in various engineering applications, such as heat exchangers, nuclear reactors, and offshore structures. In reality, the flow around cylinders may be subjected to the unbounded flow, where the effects of the neighbor structures are neglected. Besides, the bounded flow around the cylinders, where the surrounding solid wall significantly influences the flow characteristics, is also a subject of interest to researchers. This study focuses on finding the characteristics of an unbounded flow around solid bodies.

Over the past decades, a large amount of research has been devoted to extending the knowledge of the characteristics of the flow around two side-by-side cylinders with their basic shapes such as circle and square. Because these studies have provided fundamental features of the fluid dynamics surrounding the solid obstacles. Williamson (1985) experimentally investigated the flow behind a pair of circular cylinders and a pair of flat plates normal to the upstream flow. Two wake patterns such as antiphase-vortex-shedding and inphase-vortex-shedding synchronizations were discussed. For the first one, a pair of anti-phase parallel vortex streets are formed downstream, and the shape of shed vortices is conserved in the region far from the cylinders. Meanwhile, the inphase-vortex-shedding does not result in two in-phase parallel vortex streets, and the like-signed vortices merge to form larger-scale vortices. Kang (2003) numerically investigated the flow around two side-by-side circular cylinders and found six flow patterns such as 'antiphase-synchronized', 'in-phase-synchronized', 'flip-flopping', 'deflected', 'single bluff-body', and 'steady'. The flip-flopping pattern describes the switch of wide- and narrow-near wakes behind the cylinders after their several vortex

shedding. This flow pattern leads to the fluctuation of the drag coefficient of the first cylinder around the second one. The deflected pattern indicates that the wide- and narrow-near wakes are generated behind cylinders; however, their positions remain unchanged. This leads to the drag exerted on the cylinder with the narrow-near wake always being lower than that with the wide-near wake. The single bluff body pattern expresses that the vortex wake behind two cylinders is similar to the flow of a single bluff body. Nguyen and Ho (2022) numerically investigated the flow around two circular cylinders in a side-by-side arrangement with their distance varied from 1.2*D* to 6*D* at Reynolds number (*Re*) from 40 to 200. They found eight flow patterns such as 'single-buff body', 'steady', 'meandering motion', 'flip-flopping', 'deflected-in-one-direction', 'anti-phase-synchronization', 'in-phase-synchronization', and 'phase-difference-synchronization', and these patterns are strongly influenced by the *Re*, the cylinder distance and the initial external disturbance effects. The meandering motion pattern describes the meandering motion of the long shear layers behind the cylinders, and the vortices are not generated downstream because of a weak flow. Agrawal et al. (2006) examined the flow around a pair of square cylinders using the lattice Boltzmann method and pointed out the existence of both synchronized and flip-flop regimes for square cylinders, which is similar to that observed for circular cylinders. However, compared to the circular cylinders, the transition between these regimes for the square cylinder has larger spacing. It is also observed that for the slip-flopping regime, the wake behind the square cylinders is wider than another cylinder and the wake behind one cylinder is longer than another cylinder. Moreover, the probability of occurring the inphase and antiphase synchronized patterns is the same, and the time transition between the two modes lasts shorter.

Recently, the flow around elliptic cylinders is also the subject of interest because of their application in the heat exchanger industry. An elliptic cylinder has a lower resistance to the flow than the circle, and the wetted surface immersed in the fluid is higher. Therefore, the elliptic cylinders have a better heat transfer. Peng et al. (2012) numerically examined the flow around two elliptic cylinders in the side-by-side arrangement with spacing from 0.2*D* to 3*D*, *Re* from 40 to 300, and the axis ratio from 1.5 to 3. They found 'the symmetric vortex shedding mode', 'semi-single/twin vortex street formation', 'asymmetric/deflected flows', 'stationary/biased flip-flopped-type vortex shedding', 'weakly-chaotic flow', and 'in-phase/anti-phase vortex synchronizations'. However, the flow around two same-angle of attack elliptic cylinders is not clarified. This study will continue to expand the characteristics of the flow around two side-by-side elliptic cylinders at *Re* = 100 with the spacing varied from 1.2*D* to 2.5*D*. Four flow configurations, such as two normal, convergent, divergent, and same-angle-of-attack elliptic cylinders, are investigated. The vortex flow is classified into eight flow patterns, and these patterns are identified using plots of vorticity contours, and the time history of drag and lift coefficients. The flow around two elliptic cylinders is numerically simulated using the vortex-in-cell method combined with a continuous-forcing immersed boundary method (Nguyen et al., 2021). The rest of this paper is organized as follows: the numerical method is explained in Section 2, the results are discussed in Section 3, and the conclusions are finally given in Section 4.

2. Numerical method

Let D be the reference length, and the upstream velocity U_∞ be the reference velocity. The superscript '*' indicates the nondimensional. The nondimensional quantities of the flow are expressed as $\boldsymbol{x}^* = \boldsymbol{x}/D$, $\boldsymbol{u}^* = \boldsymbol{u}/U_\infty$, $t^* = tD/U_\infty$, $\nabla^* = D\nabla$, $\nabla^{*2} = D\nabla^2$, and the Reynolds (*Re*) and Froud (*Fr*) numbers are defined as $Re = U_\infty D/\upsilon$ and $Fr = U_\infty/(gD)^{1/2}$. The mass and momentum Navier–Stokes equations are written in nondimensional form for the flow of an incompressible viscous fluid as

$$\nabla^* \cdot \boldsymbol{u}^* = 0 \tag{1}$$

$$\frac{\partial \boldsymbol{u}^*}{\partial t^*} + \left(\boldsymbol{u}^* \cdot \nabla^*\right)\boldsymbol{u}^* = -\nabla^* p^* + \frac{1}{Re}\nabla^{*2}\boldsymbol{u}^* + \frac{\boldsymbol{g}^*}{Fr^2} \tag{2}$$

When taking the curl operation on both sides of Eq. (2), the momentum equation in vorticity–velocity form is expressed as

$$\frac{\partial \boldsymbol{\omega}^*}{\partial t^*} + \left(\boldsymbol{u}^* \cdot \nabla^*\right)\boldsymbol{\omega}^* = \frac{1}{Re}\nabla^{*2}\boldsymbol{\omega}^* + \left(\boldsymbol{\omega}^* \cdot \nabla\right)\boldsymbol{u}^* \tag{3}$$

where the vorticity field is defined as $\boldsymbol{\omega}^* = \nabla^* \times \boldsymbol{u}^*$. The vector velocity field is decomposed into an irrotational ve ctor field and a solenoidal vector field as

$$\boldsymbol{u}^* = \nabla^* \phi^* + \nabla^* \times \boldsymbol{\psi}^* \tag{4}$$

where ϕ^* and $\boldsymbol{\psi}^*$ are scalar and vector potentials of the velocity $\boldsymbol{u}^*$. When taking the curl operation on both sides of Eq. (4), the Poisson equation for $\boldsymbol{\psi}^*$ as

$$\nabla^{*2}\boldsymbol{\psi}^* = -\boldsymbol{\omega}^* \tag{5}$$

The Laplacian equation for ϕ^* is obtained by taking the divergence operation on both sides of Eq. (5) as

$$\nabla^{*2}\phi^* = 0 \tag{6}$$

The vortex-in-cell method discretizes the fluid into vortex particles that move at their velocity given by the flow velocity at their position and transport the flow momentum in vorticity. Equation (3) can be rewritten in the Lagrangian reference frame of vortex particles p carrying the vorticity as

$$\frac{d\boldsymbol{\omega}^*(\boldsymbol{x}_p^*)}{dt^*} = \frac{1}{Re}\nabla^2\boldsymbol{\omega}^*(\boldsymbol{x}_p^*) + \left(\boldsymbol{\omega}^*(\boldsymbol{x}_p^*)\cdot\nabla\right)\boldsymbol{u}^*(\boldsymbol{x}_p^*) \tag{7}$$

$$\frac{d\boldsymbol{x}_p^*}{dt^*} = \boldsymbol{u}^*(\boldsymbol{x}_p^*) \tag{8}$$

At the outset, the vortex particles are arranged on the regular grid nodes. Their vorticity field is updated on the mesh using Eq. (7). These vortex particles convect and transport their vorticity to the Lagrangian location by Eq. (8). Subsequently, these vortex particles are redistributed onto the initial regular grid nodes, at which their vorticity is interpolated from their value at the Lagrangian location as follows:

$$\boldsymbol{\omega}^*(\boldsymbol{x}_q^*) = \sum_{p=1}^{n_p}\boldsymbol{\omega}^*(\boldsymbol{x}_p^*)W\left(\frac{x_q^* - x_p^*}{\Delta x^*}\right)W\left(\frac{y_q^* - y_p^*}{\Delta y^*}\right) \tag{9}$$

where $W(x)$ is the third-order kernel interpolation function that is expressed as Cottet and Koumoutsakos (2000).

$$W(x)=\begin{cases}1-\frac{5}{2}|x|^2+\frac{3}{2}|x|^3 & if\ \ |x|\le 1\\ \frac{1}{2}\left(2-|x|\right)^2\left(1-|x|\right) & if\ \ 1\le|x|\le 2\\ 0 & if\ |x|>2\end{cases} \quad (10)$$

When the flow passes over a solid bluff body, the no-slip condition of the fluid flow needs to be satisfied on the solid body. This study will employ the penalization method, a continuous-forcing immersed boundary method, to enforce this condition of the flow on the body. The momentum equation, Eq. (3) can be rewritten in the penalization term to express the appearance of the solid body inside the fluid flow as

$$\frac{\partial\boldsymbol{\omega}^*}{\partial t^*}+\left(\boldsymbol{u}^*\cdot\nabla^*\right)\boldsymbol{\omega}^*=\frac{1}{Re}\nabla^{*2}\boldsymbol{\omega}^*+\left(\boldsymbol{\omega}^*\cdot\nabla^*\right)\boldsymbol{u}^* +\nabla^*\times\left(\lambda\chi_S(\boldsymbol{u}_S^*-\boldsymbol{u}^*)\right) \quad (11)$$

where λ is the penalization parameter, $\boldsymbol{u}_S$ is the solid velocity, and χ_S is the solid function that identifies the solid and fluid domains, and it is expressed as

$$\chi_S(x^*)=\begin{cases}0\ if\ x^*\in F\\ 1\ if\ \ x^*\in S\end{cases} \quad (12)$$

where F and S indicate the fluid and solid domains, respectively. To avoid numerical instability, the χ_S is smoothed in region near the fluid–solid interface using the following Heaviside function as Gazzola et al. (2011).

$$\chi_S(d)=\begin{cases}0 & if\ d<-\varepsilon\\ \frac{1}{2}\left[1+\frac{d}{\varepsilon}+\frac{1}{\pi}\sin\left(\pi\frac{d}{\varepsilon}\right)\right] & if\ \ |d|\le 1\\ 1 & if\ d>\varepsilon\end{cases} \quad (13)$$

where $d(x)$ is the signed distance from the grid node to the solid surface. The $d(x)$ is positive if x belongs to S, and $d(x)$ is negative if x belongs to F. The ε is half of the interface thickness, and it is set as $\varepsilon = 2\sqrt{2}\Delta x$. When the flow passes a solid body, a fluid force $F = (Fx, Fy)$ acts on this body. The formulas for these fluid force components Fx and Fy are followed in the research work by Nguyen and Ho (2022). Hence, the drag (Cd) and lift (Cl) coefficients of the fluid flow exerted on the solid body are expressed as follows:

$$Cd=\frac{2Fx}{\rho DU_\infty^2}\ \&\ Cl=\frac{2Fy}{\rho DU_\infty^2} \quad (14)$$

3. Results and discussions

In this study, the Poisson equation is solved using the Fourier method, where the Fourier transform is implemented using the fast Fourier transform algorithm. The Neumann boundary condition for the stream function is applied at four sides of the computational domain. The vorticity is assumed to be decayed at the outlet and far field, while the velocity at these boundaries equals the upstream velocity. The present numerical method was verified in the research work (Nguyen et al., 2021) using simulations of the flow around a single circular cylinder at Re = 100 and 200. The simulation results showed that the present numerical method captures the characteristics of the laminar flow around a solid buff body well. The convergence of the numerical method and the grid independence on the simulation results were also carried out. Therefore, the validation, and convergence study on the numerical method in this work will be omitted. We will use the best grid resolution as employed in the research work (Nguyen and Ho, 2022) to investigate the characteristics of the flow around two elliptic cylinders.

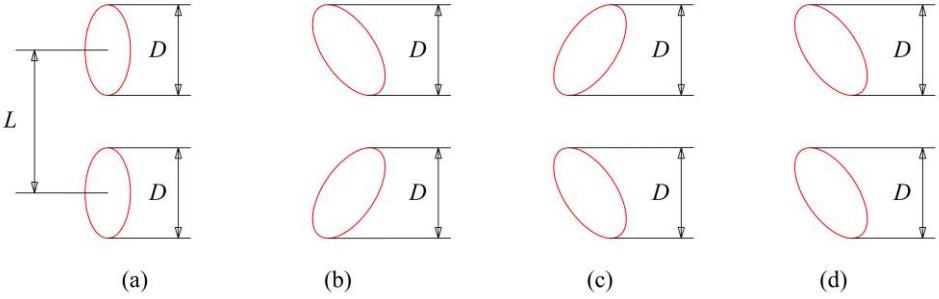

Figure 1. Configuration of flow around two side-by-side elliptic cylinders: (a) normal, (b) convergent, (c) divergent, and (d) same-angle-of-attack. Each elliptic cylinder has the axis ratio of 0.5. D is the projection of an elliptic cylinder on the vertical axis. L is the distance between centers of two cylinders

Figure 1 shows the schematics of the flow around two elliptic cylinders with four configurations such as two normal/ convergent/ divergent/ same-angle-of-attack elliptic cylinders. These elliptic cylinders have their axis ratio of 0.5. A rectangular computational domain of (-7.5D, 52.5D) × (-7.5D, 7.5D) is equally divided into 4000 × 1000 square grid cells, i.e., $\Delta x = \Delta y = 0.015D$, and the non-dimensional time step ($\Delta t^* = tD/U_\infty$) is set as 0.0025.

Figure 2 shows an instantaneous distribution of the vorticity field of the flow around two normal elliptic cylinders at Re = 100 with various spacing. At $L = 1.2D$, the inner shear layers separate from the spacing side between the cylinders. Moreover, the outer shear layers separate from the far-field sides and suppress the inner shear layers. The outer shear layers roll up to form a vortex pair like a large bubble behind the cylinders and remain unchanged with time. This flow pattern is named *steady vortex pair* (pattern A). At $L = 1.5D$, the shear layers are steady in the region near the cylinders. However, the stability of the outer shear layers breaks down and forms vortices in the middle downstream. These vortices rapidly decay to establish steady

shear layers in region far from the cylinders. Therefore, this flow pattern is named *steady shear layers followed by vortices and then a recreation of steady shear layers* (pattern B). At L = 2.0D, the vortices are shed from both sides of the cylinders and form two Karman vortex streets. These vortex streets synchronize in phase, as further demonstrated by plots of the drag and lift coefficients from the beginning to t^* = 120 shown in Fig. 3(c). Subsequently, these streets are distorted because of natural instability, and the flow is *chaotic* (pattern C). The vortices are not orderly distributed downstream, and the merging of these vortices does not occur, as observed in the pattern E. The vortex wake of the flow is not stable at this cylinder distance. Peng et al. (2012) also observed this flow pattern and pointed out that this instability is due to the intrinsic nature of the flow and not numerical errors. However, this chaotic flow is weak because of low *Re*, and it is not a turbulent flow.

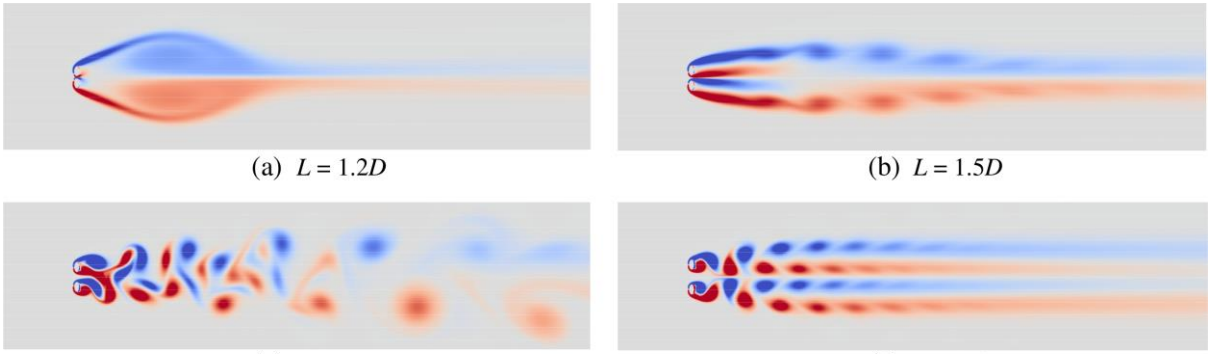

(a) L = 1.2D (b) L = 1.5D

(c) L = 2.0D (d) L = 2.5D

Figure 2. Instantaneous distribution of the vorticity field of the flow around two normal elliptic cylinders at *Re* = 100 with their spacing (a) L = 1.2D, (b) L = 1.5D, (c) L = 2.0D, and (d) L = 2.5D at t^* = 187.5

When the spacing increases as L = 2.5D, two anti-phase synchronized Karman vortex streets are formed. However, these Karman vortices rapidly decay and merge to establish steady shear layers downstream. This flow pattern is named *two anti-phase synchronized Karman vortex streets followed by steady shear layers* (pattern D).

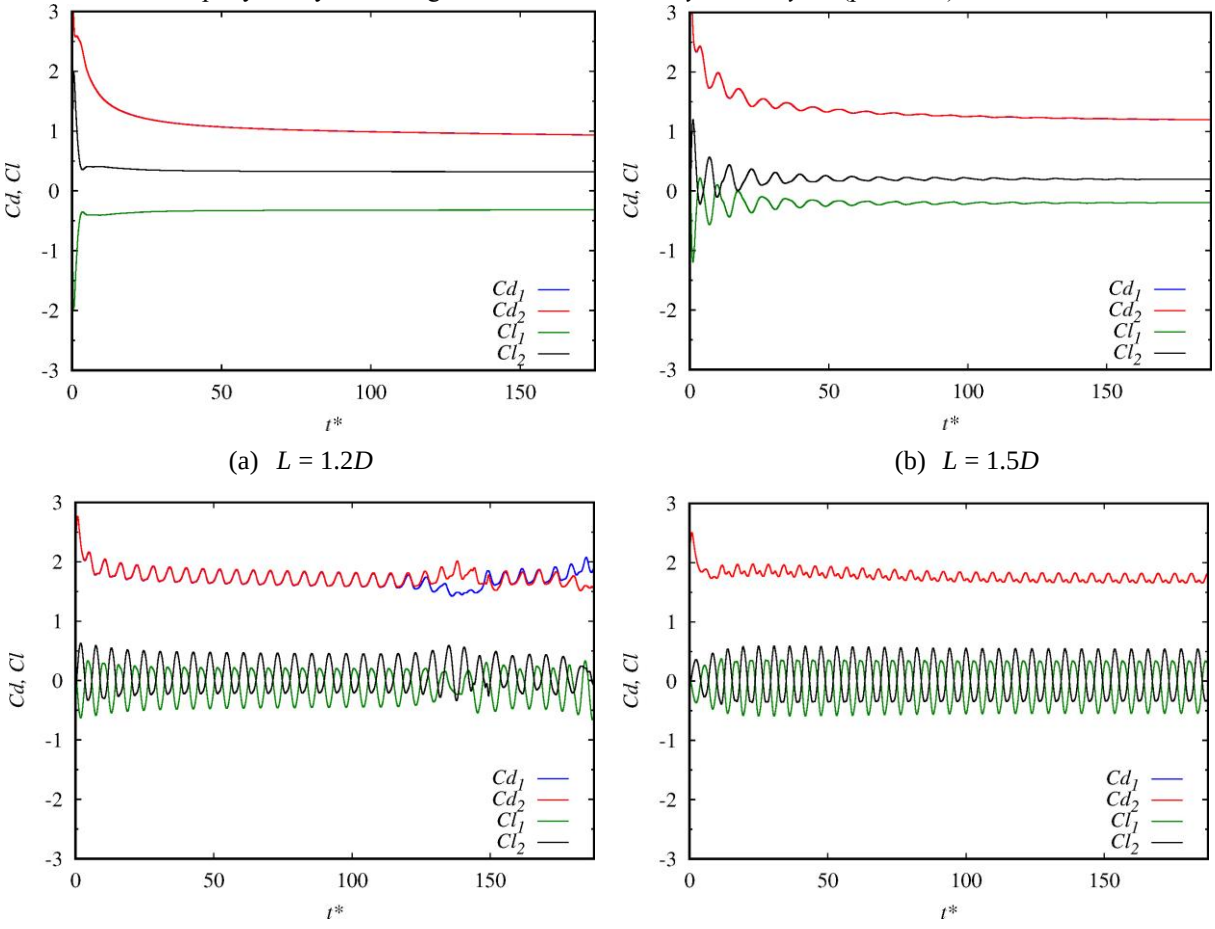

(a) L = 1.2D (b) L = 1.5D

(c) L = 2.0D (d) L = 2.5D

Figure 3. Time variation of drag and lift coefficients of the flow exerted on two normal elliptic cylinders at *Re* = 100 with their various spacing (a) L = 1.2D, (b) L = 1.5D, (c) L = 2.0D, and (d) L = 2.5D

Figure 3 describes the time variation of the drag (*Cd*) and lift (*Cl*) coefficients of the flow exerted on two normal elliptic cylinders, where scripts 1 and 2 show the lower and upper cylinders, respectively. At $L = 1.2D$, the flow is steady; therefore, the *Cd* and *Cl* of both cylinders reach constant values after the early stage of the flow. The *Cd*s of the cylinders overlap, while the *Cl*s are repulsive. At $L = 1.5D$, the *Cd* and *Cl* of the cylinders fluctuate in the early stage of the flow; however, they rapidly reach an unchanged state. This is explained by the fact that the shear layers separated from both sides of the cylinders tend to get a steady state. The *Cd* and *Cl* exerted on both cylinders are constant from $t^* = 150$. At $L = 2D$, from $t^* = 0$ to 125, the *Cd*s fluctuate in phase while the Cls fluctuate in anti-phase because of the formation of anti-phase synchronized Karman vortex streets. From $t^* = 125$, these Karman vortex streets are distorted, and the flow is chaotic. Therefore, the Cds or *Cl*s of the cylinders are not synchronous. At $L = 2.5D$, the Karman vortex streets in anti-phase are generated. The *Cd*s of the cylinders fluctuate in phase, while the *Cl*s synchronize in anti-phase.

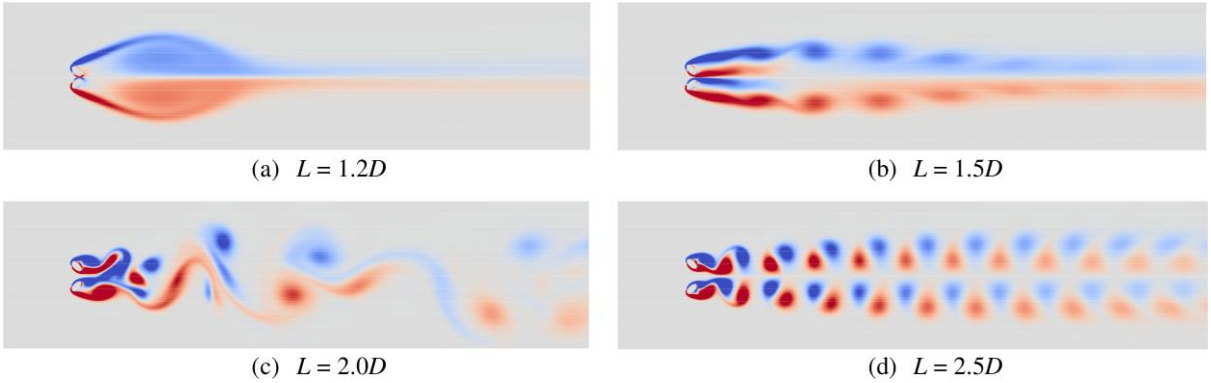

(a) $L = 1.2D$ (b) $L = 1.5D$

(c) $L = 2.0D$ (d) $L = 2.5D$

Figure 4. Instantaneous distribution of the vorticity field of the flow around two convergent elliptic cylinders at $Re = 100$ with their spacing (a) $L = 1.2D$ at $t^* = 150$, (b) $L = 1.5D$ at $t^* = 187.5$, (c) $L = 2.0D$ at $t^* = 187.5$, and (d) $L = 2.5D$ at $t^* = 187.5$

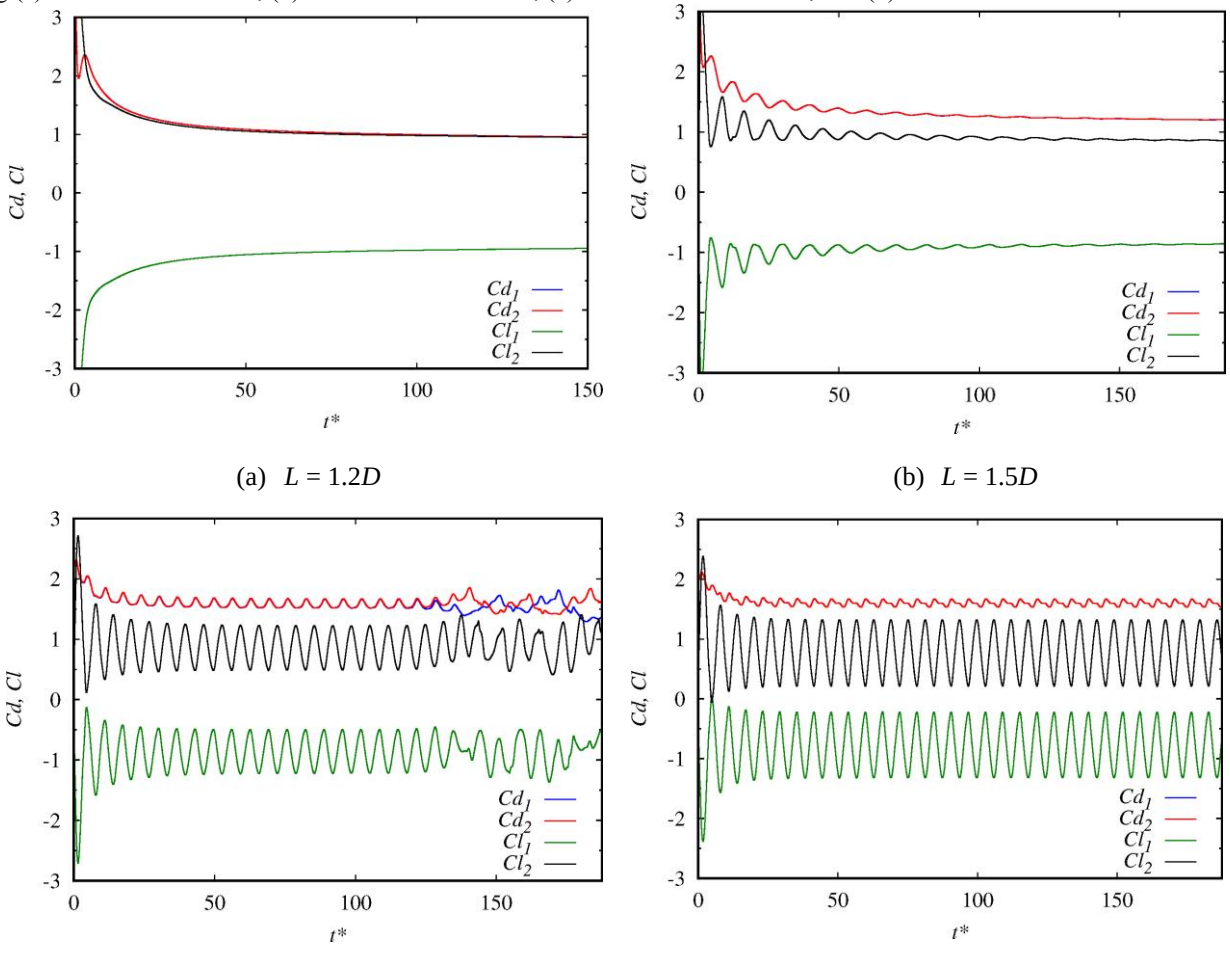

(a) $L = 1.2D$ (b) $L = 1.5D$

(c) $L = 2.0D$ (d) $L = 2.5D$

Figure 5. Time history of drag and lift coefficients of the flow exerted on two convergent elliptic cylinders at $Re = 100$ with their various spacing (a) $L = 1.2D$, (b) $L = 1.5D$, (c) $L = 2.0D$, and (d) $L = 2.5D$

Figure 4 shows the instantaneous distribution of the vorticity field of the flow around two convergent elliptic cylinders with their various spacing. At $L = 1.2D$ and $1.5D$, the behaviors of the wake behind the cylinders are the same as those of two normal elliptic cylinders. At $L = 2.0D$, the merging of shed vortices to form large eddies of low frequency instantly occurs in region near behind the cylinders. Moreover, the wide- and narrow-near wakes are observed behind the lower and upper cylinders, respectively. Note that the near wake indicates the wake just behind the cylinder, and the 'wide' and 'narrow' expresses the size of the near wake in the vertical direction. The position of these wakes is switched after several vortex shedding, as discussed further later. This flow pattern is named *flip-flopping wake* (pattern E). At $L = 2.5D$, *two anti-phase synchronized Karman vortex streets* (pattern F) are generated downstream. Interestingly, the shape of the Karman vortices is conserved downstream far from the cylinders.

Figure 5 shows the time variation of the drag and lift coefficients of the flow acting on two convergent elliptic cylinders. The *Cd*s and *Cl*s of the cylinders at $L = 1.2D$ and $1.5D$ are similar to those in the cases with two normal cylinders. At $L = 2.0D$, the repulsiveness of *Cl*s of the cylinders exists, while *Cd*s of the cylinders overlap from the beginning to $t^* = 130$. From $t^* = 130$, the Cd_1 fluctuates around the Cd_2 after several vortex shedding. This is explained by switching near wakes behind two cylinders. At $L = 2.5D$, the *Cd*s fluctuate in phase, while the *Cl*s oscillate in anti-phase. This further proves the anti-phase synchronization of the vortex streets behind the cylinders.

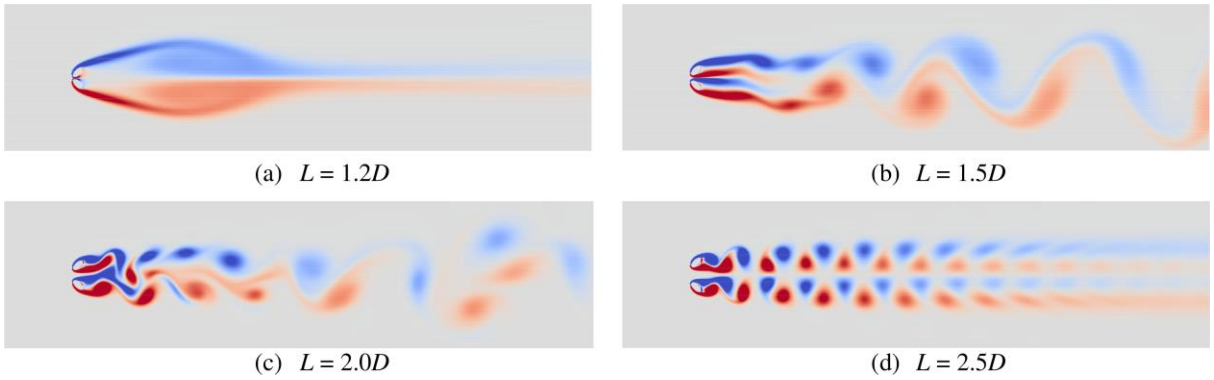

(a) $L = 1.2D$ (b) $L = 1.5D$

(c) $L = 2.0D$ (d) $L = 2.5D$

Figure 6. Instantaneous distribution of the vorticity field of the flow around two divergent elliptic cylinders at $Re = 100$ with their spacing (a) $L = 1.2D$ at $t^* = 187.5$, (b) $L = 1.5D$ at $t^* = 187.5$, (c) $L = 2.0D$ at $t^* = 175$, and (d) $L = 2.5D$ at $t^* = 187.5$

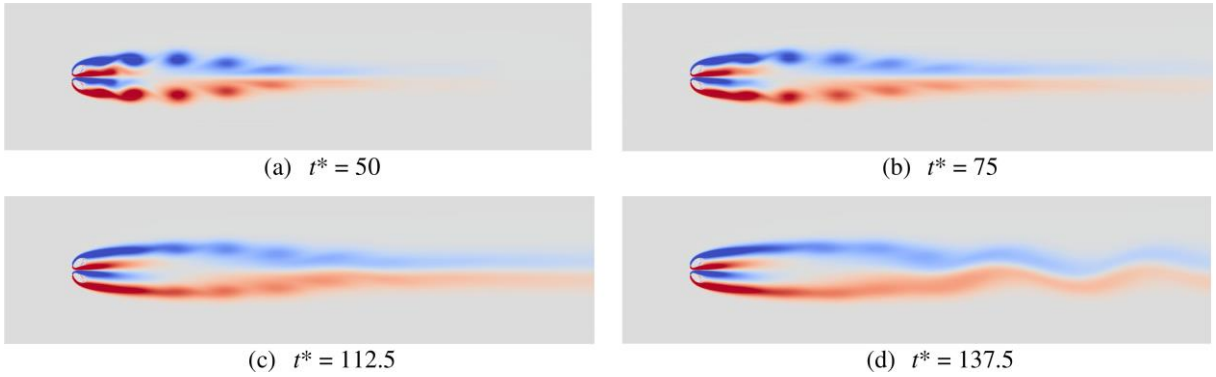

(a) $t^* = 50$ (b) $t^* = 75$

(c) $t^* = 112.5$ (d) $t^* = 137.5$

Figure 7. Time variation of the vortex wake of flow around two divergent elliptic cylinders at $Re = 100$ with their spacing $L = 1.5D$ at (a) $t^* = 50$, (b) $t^* = 75$, (c) $t^* = 112.5$, and (d) $t^* = 137.5$

Figure 6 describes an instantaneous distribution of the vorticity field of the flow around two divergent elliptic cylinders. The steady vortex pair pattern takes place at $L = 1.2D$, as observed with two normal/convergent elliptic cylinders. At $L = 1.5D$, shear layers separated from the cylinders are steady. These shear layers roll up to form a Karman vortex street downstream. Therefore, this flow pattern is named *steady shear layers followed by a Karman vortex street* (pattern G), as further expressed later. The *flip-flopping wake* (pattern E) occurs at $L = 2.0D$, while the *two anti-phase synchronized Karman vortex streets followed by steady shear layers* (pattern D) is observed at $L = 2.5D$.

Time evolution of pattern G (*steady shear layers followed by a Karman vortex street*) is further clarified in Figure 7. At $t^* = 50$, the outer shear layers roll up to form vortices. These vortices decay to generate two shear layers as the wake develops at $t^* = 75$ and 112.5. These shear layers under the natural instability roll up to form vortices, as seen at $t^* = 137.5$, resulting in a Karman vortex street, as seen in Fig. 6(b).

Figure 8 shows the time evolution of the *Cd* and *Cl* of the flow exerted on two divergent elliptic cylinders. At $L = 1.2D$ and $1.5D$, the shear layers are steady; therefore, the *Cd* and *Cl* of the cylinders reach constant values after the early flow stage. At $L = 2.0D$, the *flip-flopping* phenomena happen, in which the wide- and narrow-near wakes behind the cylinders switch together after several vortex shedding. This is proved the fact

that the Cd_1 fluctuates around Cd_2 after several vortex shedding. At $L = 2.5D$, the Cd_1 and Cd_2 overlap, while the Cl_1 and Cl_2 are repulsive and in anti-phase. This further demonstrates the characteristics of pattern D (*two anti-phase synchronized Karman vortex streets followed by steady shear layers*) as described above.

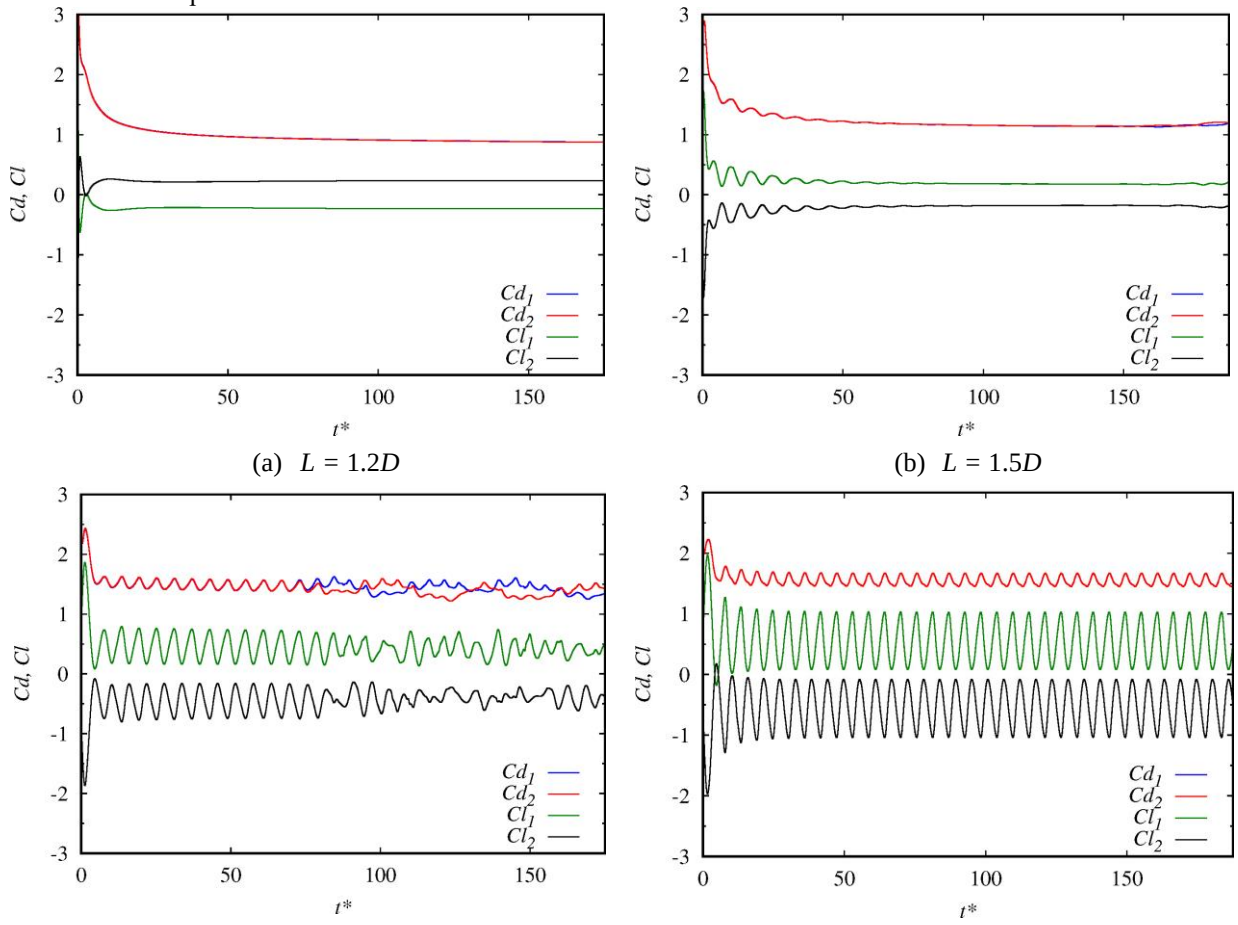

(a) $L = 1.2D$ (b) $L = 1.5D$

(c) $L = 2.0D$ (d) $L = 2.5D$

Figure 8. Time variation of drag and lift coefficients of the flow exerted on two divergent elliptic cylinders at $Re = 100$ with their various spacing (a) $L = 1.2D$, (b) L = $1.5D$, (c) $L = 2.0D$, and (d) $L = 2.5D$

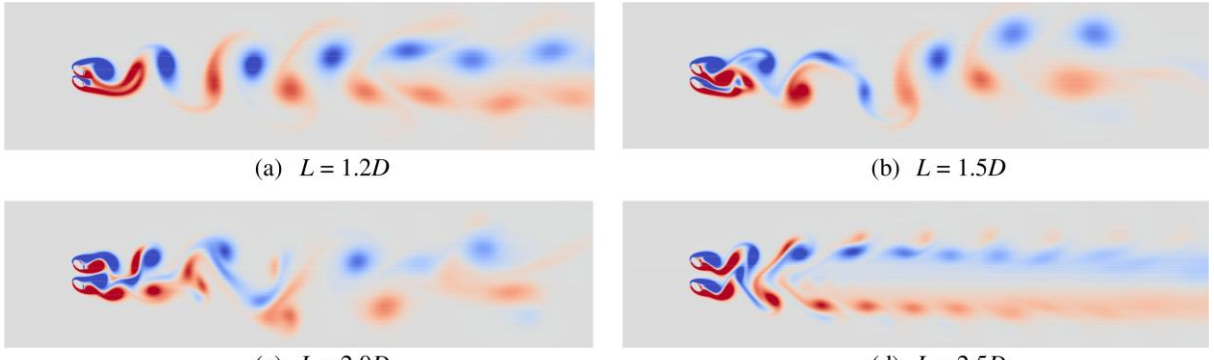

(a) $L = 1.2D$ (b) $L = 1.5D$

(c) $L = 2.0D$ (d) $L = 2.5D$

Figure 9. Instantaneous distribution of the vorticity field of the flow around two same-angle-of-attack elliptic cylinders at $Re = 100$ with their spacing (a) $L = 1.2D$ at $t^* = 212.5$, (b) $L = 1.5D$ at $t^* = 137.5$, (c) $L = 2.0D$ at $t^* = 200$, and (d) $L = 2.5D$ at $t^* = 187.5$

Figure 9 describes an instantaneous distribution of the vorticity field of the flow around two same-angle-of-attack elliptic cylinders. At $L = 1.2D$, the vortex wake generated from the cylinders is similar to the flow around a *single bluff body* (pattern H). A Karman vortex street is formed behind the cylinders. However, this vortex street is distorted in the region far from the cylinders. At $L = 1.5D$ and $2.0D$, the *flip-flopping wake* (pattern E) occurs. It is clear that the flow pattern at this configuration is more unstable than at three configurations, as discussed above. Because this flip-flopping phenomena only take place at $L = 1.5D$ for the case of two same-angle-of-attack elliptic cylinders. At $L = 2.5D$, *two in-phase synchronized vortex streets* (pattern I) are formed. However, at this flow pattern, vortices rapidly decay downstream because of the merging of like-signed vortices.

Figure 10 expresses the time evolution of the Cd and Cl of the flow exerted on two same-angle-of-attack elliptic cylinders. At $L = 1.2D$, the *single bluff body flow* occurs, the Cd_1 and Cd_2,

the Cl_1 and Cl_2 fluctuate in phase. The time averaged Cd_1 is similar to that of Cd_2. At L = 1.5D and 2.0D, the *flip-flopping* happens, the Cd_1 oscillates around Cd_2 after several vortex shedding. At L = 2.5D, the fluctuation of Cl_1 and Cl_2 is in-phase. The fluctuation amplitude of Cl of the upper cylinder is much higher than the lower one.

Table 1. Root mean square (rms) of lift coefficients of lower (Cl_1) and upper (Cl_2) cylinders

Flow configuration	rms	L = 1.2D	1.5D	2.0D	2.5D
Normal	rms_Cl_1 = rms_Cl_2	0	0	0.244	0.326
Convergent		0	0	0.243	0.378
Divergent		0	0	0.15	0.335
Same-angle-of-attack	rms_Cl_1	0.09	0.087	0.142	0.135
	rms_Cl_2	0.184	0.215	0.284	0.311

Table 1 shows the root mean square of the lift coefficients (rms_Cl) of the lower and upper cylinders. The rms_Cl is calculated as

$$\text{rms\_}Cl = \sqrt{\sum_{i=1}^{i=N_{\Delta t}} \left(Cl(t) - \overline{Cl}\right)^2 / N_{\Delta t}} \qquad (15)$$

where $\overline{Cl} = \sum_{i=1}^{i=N_{\Delta t}} Cl(t) / N_{\Delta t}$ and $N_{\Delta t}$ is the total time step after the early development stage of the flow. From the table, it is observed that rms_Cl at L = 1.2D and 1.5D for the normal, convergent, divergent configurations is zero because of the steady shear layer behind the cylinders. However, the rms_Cl at these spacing for the same-angle-of-attack configuration appears. The flow in the same-angle-of-attack configuration is steady at the low spacing. When the spacing increase, the rms_Cl increases. The rms_Cl_1 is equal to the rms_Cl_2 for the normal, convergent and divergent configurations, while they do not occur for the same-angle-of-attack one. In particular, the rms_Cl_2 is twice the rms_Cl_1 because of the asymmetric configuration.

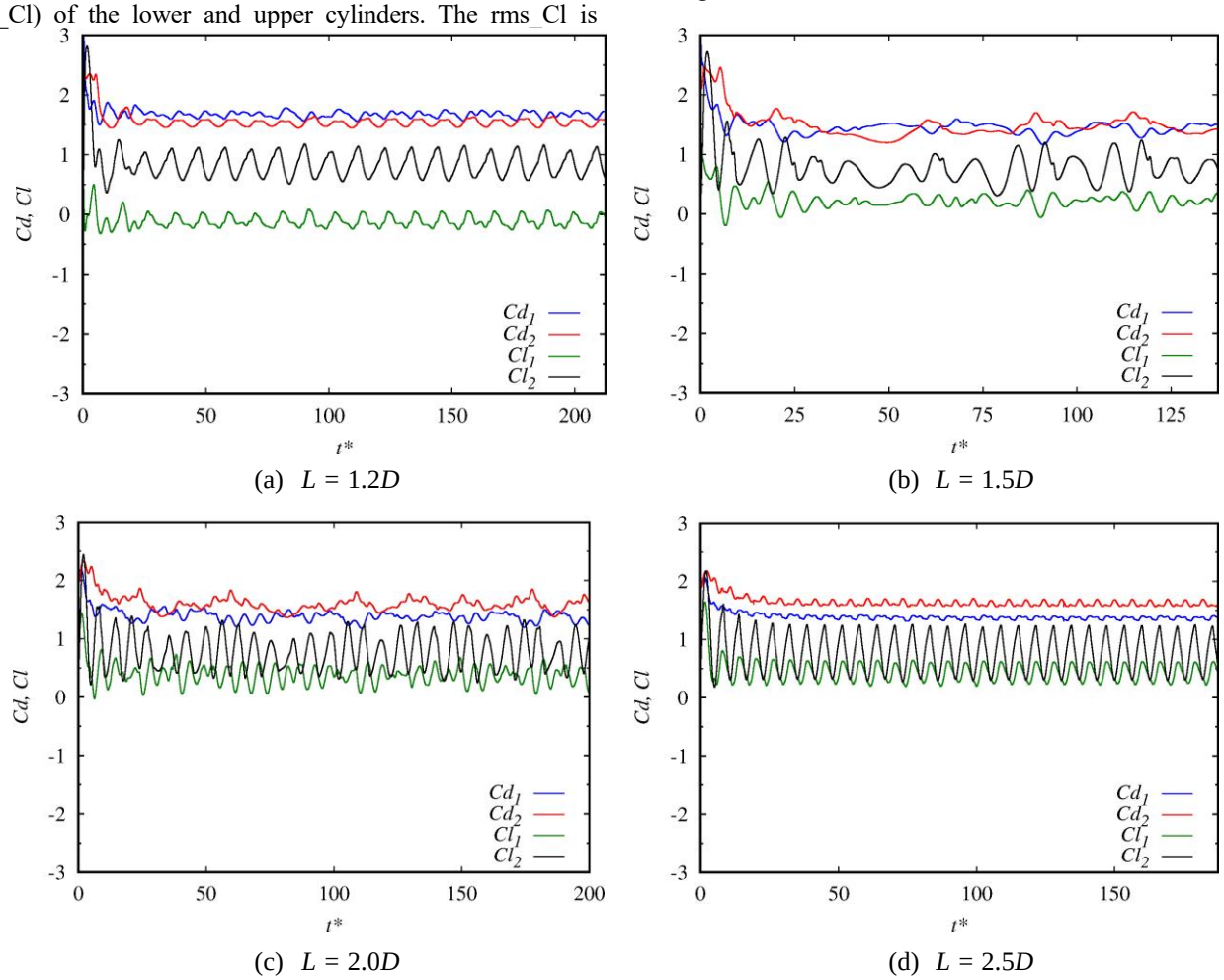

(a) L = 1.2D (b) L = 1.5D

(c) L = 2.0D (d) L = 2.5D

Figure 10. Time variation of drag and lift coefficients of the flow exerted on two same-angle-of-attack elliptic cylinders at Re = 100 with their various spacing (a) L = 1.2D , (b) L = 1.5D, (c) L = 2.0D, and (d) L = 2.5D

4. Conclusions

Characteristics of the vortex wake of the flow around two elliptic cylinders with various configurations at Re = 100 were numerically investigated using a vortex-in-cell method combined with a continuous-forcing immersed boundary method. The vortex wakes of the flow around two elliptic cylinders are classified into nine patterns as steady vortex pair, a single bluff body flow, two anti-phase synchronized Karman vortex streets, two in-phase synchronized vortex streets, two anti-phase synchronized Karman vortex streets followed by steady shear layers, steady shear layers followed by vortices and then a recreation of steady shear layers, steady shear layers

followed by a Karman vortex street, flip-flopping wake, and chaotic flow. These pattern significantly depend on the spacing between two cylinder centers and their configuration. The root mean square of the lift coefficient (rms_*Cl*) increases as the cylinder spacing rises. The rms_Cl_1 equals rms_Cl_2 for the normal, convergent, divergent configurations, while it does not take place for the same-angle-of-attack configuration. Moreover, the rms_Cl_2 is almost twice the rms_Cl_1 for the whole investigated spacing.

REFERENCES

Agrawal, A., Djenidi, L. and Antonia, R.A. (2006), "Investigation of flow around a pair of side-by-side square cylinders using the lattice Boltzmann method", *Computers & Fluids*, Vol. 35 No. 10, pp. 1093-1107. doi:https://doi.org/10.1016/j.compfluid.2005.05.008

Cottet, G.H. and Koumoutsakos, P.D. (2000), *Vortex Methods: Theory and Practice*, Cambridge University Press.

Gazzola, M., Chatelain, P., van Rees, W.M. and Koumoutsakos, P. (2011), "Simulations of single and multiple swimmers with non-divergence free deforming geometries", *Journal of Computational Physics*, Vol. 230 No. 19, pp. 7093-7114. doi:https://doi.org/10.1016/j.jcp.2011.04.025

Kang, S. (2003), "Characteristics of flow over two circular cylinders in a side-by-side arrangement at low Reynolds numbers", *Physics of Fluids*, Vol. 15 No. 9, pp. 2486-2498. doi:10.1063/1.1596412

Nguyen, V.L. and Ho, D.K. (2022), "Numerical investigation of vortex wake patterns of laminar flow around two side-by-side cylinders", *Archive of Mechanical Engineering*, Vol. vol. 69 No. No 3, pp. 541-565. doi:10.24425/ame.2022.141517

Nguyen, V.L., Nguyen-Thoi, T. and Duong, V.D. (2021), "Characteristics of the flow around four cylinders of various shapes", *Ocean Engineering*, Vol. 238, pp. 109690. doi:https://doi.org/10.1016/j.oceaneng.2021.109690

Peng, Y.F., Sau, A., Hwang, R.R., Yang, W.C. and Hsieh, C.-M. (2012), "Criticality of flow transition behind two side-by-side elliptic cylinders", *Physics of Fluids*, Vol. 24 No. 3, pp. 034102. doi:10.1063/1.3687450

Williamson, C.H.K. (1985), "Evolution of a single wake behind a pair of bluff bodies", *Journal of Fluid Mechanics*, Vol. 159, pp. 1-18. doi:10.1017/S002211208500307X